

Bacterial cellulose nanocrystals: impact of the sulfate content on the interaction with xyloglucan

Cleverton Luiz Pirich · Rilton Alves de Freitas · Marco Aurelio Woehl ·
Guilherme Fadel Picheth · Denise F. S. Petri · Maria Rita Sierakowski

Received: 21 August 2014 / Accepted: 6 April 2015 / Published online: 9 April 2015
© Springer Science+Business Media Dordrecht 2015

Abstract In the present work, bacterial cellulose nanocrystals (BCN) were prepared with three distinct sulfate contents, namely 0, 0.42 and 0.65 % OSO_3^- , by using HCl (BCN-HCl), a mixture of HCl and H_2SO_4 (BCN-HCl/ H_2SO_4) and H_2SO_4 (BCN- H_2SO_4) as hydrolytic media, respectively. BCN were characterized by means of elemental analysis, X-ray diffraction, atomic force microscopy (AFM) and zeta potential measurements. All BCN samples had crystallinity indices of about 82 %, about 10 % higher than the original BC. The zeta potential values determined for BCN-HCl, BCN-HCl/ H_2SO_4 and BCN- H_2SO_4 amount-

ed to $-(5 \pm 1)$, $-(40 \pm 1)$ and $-(46 \pm 1)$ mV, respectively. The assembly between BCN-HCl, BCN-HCl/ H_2SO_4 or BCN- H_2SO_4 and XG extracted from *Tamarindus indica* seeds was investigated by means of Freundlich isotherms, AFM, contact angle measurements, dynamic light scattering, ellipsometry and quartz crystal microbalance measurements. The adsorption experiments suggest that sulfate substitution on BCN surface as low as 0.65 % OSO_3^- impairs the original interaction with XG, thereby generating unstable layers with subsequent desorption. In contrast, the 0.42 % OSO_3^- samples presented favorable interactions with XG and exhibited highly improved colloidal stability compared to 0 % OSO_3^- samples. Films of XG adsorbed onto BCN with 0.42 % OSO_3^- were stable, homogeneous, and had low roughness and thickness. This is the first report showing that sulfate content on BCN surface can be tailored to promote high colloidal stability and sufficient interaction with XG.

Electronic supplementary material The online version of this article (doi:10.1007/s10570-015-0626-y) contains supplementary material, which is available to authorized users.

C. L. Pirich · R. A. de Freitas · M. A. Woehl ·
G. F. Picheth · M. R. Sierakowski (✉)
BioPol, Chemistry Department, Federal University of
Paraná, P.B. 19032, Centro Politécnico,
CEP 81531-980 Curitiba, Brazil
e-mail: mariarita.sierakowski@ufpr.br;
mariarita.sierakowski@gmail.com

C. L. Pirich
Biochemistry and Molecular Biology Department, Federal
University of Paraná, Centro Politécnico,
CEP 81531-980 Curitiba, PR, Brazil

D. F. S. Petri
Institute of Chemistry, University of São Paulo,
CEP 05508-000 São Paulo, Brazil

Keywords Sulfate content · Adsorption · Bacterial cellulose nanocrystals · Xyloglucan · Thin films

Introduction

The development of environmentally friendly and sustainable materials is of great interest for industrial and scientific applications due to the use of materials from renewable sources. Among the potential candidates for biomedical devices, the combined use of

cellulose and xyloglucan (XG) has great advantages due to their low toxicity, abundance in nature, easy chemical functionalization, good mechanical performance and strong chemical interactions (Karaaslan et al. 2011; Kummerer et al. 2011; Shirakawa et al. 1998; Zhou et al. 2007). The high affinity between cellulose and XG is mainly due to the high content of hydrogen bonds between the similar backbone structures of these polysaccharides (*D*-anhydroglucopyranose chains bonded through β -(1 \rightarrow 4) linkages) and hydrophobic interactions (Morris et al. 2004). Additionally, XG backbone is partially substituted with α -*D*-Xyl side-chains at the O-6 atoms and, depending on the source, the side-chains can be composed of β -*D*-Gal-1,2- α -*D*-Xyl, α -*L*-Fuc-1,2- β -*D*-Gal-1,2- α -*D*-Xyl (Carpita and Gibeau 1993; Fry 1989; Hayashi 1989; McNeil et al. 1984), or more complex chains (Freitas et al. 2005; Hantus et al. 1997; Jia et al. 2003; York et al. 1996).

In nature, cellulose and XG are found in plant cell walls associated in a supramolecular structure, which promotes resistance and viscoelasticity in woods (Mellerowicz et al. 2008). Cellulose nanocrystals exhibit increased crystallinity index (up to 10 %) and elasticity (Young's modulus up to 100 GPa) in comparison to intact cellulose (Hsieh et al. 2008; Iguchi et al. 2000). The interaction between cellulose nanocrystals and XG improves colloidal and thermal stability, extensibility and Young's modulus of the resultant biocomposites (Cerclier et al. 2010; Eronen et al. 2011; Jean et al. 2009; Lima et al. 2004; Lopez et al. 2010; Souza et al. 2013; Whitney et al. 1999). Furthermore, XG subunits like galactose can be selectively modified to obtain substances with new applications, such as substrates for peptide-immobilization, anticoagulant and antithrombotic agents (Doliška et al. 2012; Parikka et al. 2012).

The crystalline domains of cellulose can be isolated by several chemical, mechanical and/or enzymatic treatments, to generate materials with distinct properties (dimensions, morphology, crystallinity and surface chemical substitution), which in turn can affect the interaction with XG (Filson et al. 2009; Kalashnikova et al. 2011; Martínez-Sanz et al. 2011). Sulfuric acid hydrolysis is the most common technique because it produces cellulose crystals that are dispersible in water due to the sulfate ester groups introduced on the surface during hydrolysis (Ranby et al. 1949).

The use of sulfuric acid is due to simplicity, lower cost and, notably, obtainment of particles with high colloidal stability. In such reaction, the hydronium ions penetrate the cellulose's amorphous domains, promoting the hydrolytic cleavage of the glycosidic bonds and releasing individual crystallites. In this process, sulfate groups are randomly distributed on the cellulose surface (Dong et al. 1998; Marchessault et al. 1959). Under optimized conditions, crystals with controlled polydispersity and high amounts of sulfate groups can be obtained (Bondeson et al. 2006; Lin and Dufresne 2014a; Martínez-Sanz et al. 2011).

Besides the improvement of colloidal stability through sulfate esterification on cellulose crystals, the sulfate introduction results in products with poor thermal stability (maximum degradation temperature, T_{\max} , of 250 °C), which prevents using these crystals to make products through several melt processing techniques, such as injection molding, twin-screw compounding and extrusion (Ben Azouz et al. 2011; Oksman et al. 2006).

Lopez et al. (2010) demonstrated that very low sulfate content (≤ 0.033 %) on cellulose crystals' surface did not significantly affect the adsorption of XG onto cellulose, although sulfated cellulose crystals exhibited slightly lower adsorption when compared to desulfated. However, in order to obtain cellulose crystals with minimum colloidal stability and/or a narrow size distribution, several authors have used sulfuric hydrolysis under more drastic conditions (longer time, higher temperatures or acid concentration), yielding up to 0.2 % of sulfate content (Bondeson et al. 2006; Lin and Dufresne 2014a; Martínez-Sanz et al. 2011). Moreover, other properties of cellulose crystals (e.g., size distribution, morphology and crystallinity) can significantly alter the adsorption to XG (Zhao et al. 2014). Even adsorption conditions like polymer critical concentration or production by spin-coating, solvent-casting and spraying techniques could engender different adsorption forces, e.g. centrifugal force (Cerclier et al. 2010).

In this study, the influence of sulfate esterification levels on cellulose crystals of bacterial cellulose (BCN) on the interaction with XG was investigated in dispersion and in self-assembled systems composed of single or multiple layers, deposited by the layer-by-layer (LbL) technique (Iler 1966). From the fundamental point of view, the results presented here allow

evaluating the impact of high sulfate content ($>0.1\%$) on BCN surface in respect to XG adsorption. Especially in aqueous systems, where sulfate groups play an important role for colloidal stability due to the electrostatic repulsion, the results could enable more efficient self-assembly BCN-XG particles, which could be applied in different areas, such as improvement of cellulose surface capability to immobilize biomolecules, biosensor build-up and for emulsion stabilization (e.g., Pickering emulsions).

Materials and methods

Materials

Pieces of dried bacterial cellulose (BC) sheets were kindly provided by Membracel[®] Produtos Tecnológicos Ltda. (Almirante Tamandaré, Paraná, Brazil). The xyloglucan (XG) from *T. indica* seeds (Balasanka Mills, India), as purified and characterized by Jó et al. (2010), had weight-average molar mass (M_w), dispersity (M_w/M_n) and overlap concentration (c^*), determined by a steric exclusion chromatograph connected to a laser light scattering detector (model 270 Dual Detector Viscotek), of $653,000\text{ g mol}^{-1}$, 1.05, and 1.38 mg mL^{-1} , respectively. H_2SO_4 (95–98 % w/w—Sigma Aldrich[®]) and HCl (37 % w/w—Merck) were used for BC hydrolysis to obtain BCN. Polyethyleneimine (PEI) (Polymin[®] SNA) was used as the anchoring substrate in the LbL assays. Ultrapure water ($18.2\text{ M}\Omega\text{ cm}$, Millipore Milli-Q purification system) was used to prepare aqueous BC and BCN suspensions and XG and PEI solutions.

Pretreatment of bacterial cellulose

Pieces of dried bacterial cellulose sheets were suspended in water using a mechanical mixer (Philips-Walita, 400 W) and were then ground in a supermass colloid mill (Masuko Sangyo MKCA6-2). After mechanical treatment, each sample (8 mg mL^{-1}) was submitted to ultrasound in an ice bath for 60 min using an ultrasonic processor (Sonics VCX 750 at 20 kHz). One drop of CHCl_3 per 250 mL was added to the suspension for storage and kept at $4\text{ }^\circ\text{C}$ until use (Kalashnikova et al. 2011).

Obtaining bacterial cellulose nanocrystals (BCN)

The pretreated cellulose suspension at 8 mg mL^{-1} was submitted to acid hydrolysis under three different conditions. For the sulfate-free sample (BCN-HCl), HCl (4 mol L^{-1}) at the temperature of $80\text{ }^\circ\text{C}$ for 120 min was applied (Yu et al. 2013); for the moderate sulfate content sample (BCN-HCl/ H_2SO_4), a mixture composed of $\text{H}_2\text{O}:\text{H}_2\text{SO}_4:\text{HCl}$ in a proportion of 6:2.5:1.5 (v/v) was heated at $60\text{ }^\circ\text{C}$ for 120 min (adapted from Zhang et al. 2007); and for the high sulfate content sample (BCN- H_2SO_4), H_2SO_4 (5.2 mol L^{-1}) was heated at $50\text{ }^\circ\text{C}$ for 120 min (Martínez-Sanz et al. 2011). All the suspensions were rinsed with ultrapure water using repeated centrifuge cycles of 10 min at $10,000g$ (Sigma 4K15), i.e., the supernatant was removed from the sediment and replaced by fresh ultrapure water and mixed. The centrifuge step was stopped at $\text{pH} > 4$, when the supernatant became turbid. The supernatant was dialyzed against ultrapure water to remove any remaining free acid until the collecting medium water reached the same conductivity as the ultrapure water. Afterward, the dispersions were sonicated (Ultracleaner 1650A) for 10 min and stored at $4\text{ }^\circ\text{C}$ with one drop of CHCl_3 per 250 mL (Kalashnikova et al. 2011).

Sulfur content of the BCN samples

Sulfur content in the lyophilized BCN powder samples (10 mg) was determined by inductively coupled plasma atomic emission spectroscopy (ICP-AES) using a Spectro spectroscopy (Spectro Analytical Instruments GmbH, Germany). The atomic emission intensity of sulfur in each sample (10 mg, in triplicate) was recorded at a wavelength of 180.7 nm, after concentrated nitric acid digestion; the sulfur content was measured and related to total mass.

X-ray powder diffraction (XRPD) analysis

For the BC and BCN samples suspended in water, the solvents were exchanged with tert-butanol using a stepwise gradient to minimize recrystallization and change of the crystallinity index of the cellulose chains (Ramos et al. 1993; Woehl et al. 2010). The

last washing step was performed with pure tert-butanol. The fiber suspension of each sample was centrifuged for 10 min at 10,000g, and the recovered fibers were lyophilized in a bench-top freeze-drier (Thermo Electron Corporation). The XRPD experiments were performed in a Shimadzu XRD 6000 diffractometer operating at 40 kV and 30 mA with Cu K α radiation ($\lambda = 0.15418$ nm). The lyophilized samples were positioned on an aluminum sample holder, and measurements were taken to estimate the crystallinity, as described previously by Chen et al. (2007). Data were collected in reflectance mode in the 10–40° 2 θ -range with 0.5° min⁻¹. The diffractograms were fitted with the Gaussian model (Fityk 0.8.0). The crystallinity index (CrI, %) was calculated using the following method, as described by Hermans (1946):

$$CrI(\%) = 100 \cdot \frac{A_c}{A_t} \quad (1)$$

where A_c corresponds to the total crystalline area and A_t is the total area (amorphous and crystalline) under the diffractograms.

The peaks were also used to estimate the apparent crystal size (ACS), using Scherrer's formula according to the following equation:

$$ACS = \frac{0.9 \lambda}{FWHM \cos \theta} \quad (2)$$

where λ is the X-ray wavelength expressed in nm, FWHM is the peak width at half the maximum height and θ is the diffraction angle expressed in radians. The form factor (0.9) is valid for spherical particles, which does not pose a problem because the results were used only for comparative purposes. To verify the curve resolution program routine and indexation of diffractograms, they were compared with crystal information file (.cif) for different cellulose polymorphs from supplementary material of French (2014), using the Mercury software (version 3.3). The d spaces between the crystal planes were determined using Bragg's law:

$$n \lambda = 2 d \sin \theta \quad (3)$$

where n is an integral number (1, 2, 3...), and d represents the intersegment spacing between two polymer chains.

Freundlich isotherm analysis of XG adsorption on BCN

Adsorption experiments of XG, in the concentration range of 200–500 $\mu\text{g mL}^{-1}$, onto BCN at constant concentration of 1 mg mL^{-1} were performed at $(25 \pm 1)^\circ\text{C}$. In order to avoid aggregation between BCN particles, all BCN solutions were previously sonicated for 10 min before adding XG. After incubation with continuous head-over-tail mixing at $(25 \pm 1)^\circ\text{C}$ for 30 min, the blends were centrifuged for 30 min at 13,000g (Sigma 4K15), and the amount of XG unbound to BCN present in the supernatant was quantified by the I₂/KI colorimetric method (Kooiman 1960). The centrifugation was necessary to precipitate all BCN and BCN bound to XG, whereas unbound XG remained free in solution (adapted from Lima and Buckeridge 2001). The adsorption of XG onto BCN was evaluated following the Freundlich empirical model:

$$Q_e = m C_e^{1/n} \quad (4)$$

where C_e is the amount of XG unbound to BCN quantified in the supernatant after centrifugation, Q_e is the mass (μg) of XG adsorbed per mg of cellulose, m is a complex function describing both the maximum capacity and the average binding affinity and $1/n$ is the surface heterogeneity index, which varies from 0 for heterogeneous systems to 1 for homogeneous systems. The surface heterogeneity index depends on the surface properties, the crystallinity degree and the distribution of active adsorption sites.

The experimental binding isotherm data fitted the linear form of Eq. 4:

$$\ln(Q_e) = \ln(m) + \frac{1}{n} \ln(C_e) \quad (5)$$

The graph of $\ln(Q_e)$ versus $\ln(C_e)$ provided $\ln(m)$ as intercept and $1/n$ as slope.

Dynamic light scattering (DLS) analysis of polysaccharides

The colloidal stability of BCN particles was assessed by monitoring the average apparent hydrodynamic diameter as a function of time, with a nano DLS laser light-scattering apparatus from Brookhaven

Instruments (Holtville, New York) operating at the fixed angle of 90° and wavelength at 632.8 nm, provided by a 15 mW solid-state He–Ne laser. All BCN samples were sonicated for 10 min prior to injection. All measurements were performed at 25°C in triplicate. The values of the diffusion coefficient (D) were obtained from the autocorrelation functions and correlated with the Stokes–Einstein equation:

$$D_h = \frac{K_B T}{3 \pi \eta D} \quad (6)$$

where D_h is the hydrodynamic diameter, K_B is the Boltzmann constant, T is the temperature and η is the viscosity (Berne and Pecora 2000).

The Stokes–Einstein equation can be applied only for non-interacting spherically shaped particles. Thus the D_h values of BCN are not expected to be equal to the length or width of actual particles; they only correlate with the average effective particle movement within a liquid. For this reason, D_h stands for the average apparent hydrodynamic diameters (D_{happ}), which can be used comparatively to evaluate the colloidal stability.

Zeta potential analysis

The zeta potential (ζ) values were measured with a Zetasizer Nano ZS (Malvern Instruments) based on the LDV technique (Laser Doppler Velocimetry). A DTS 1060c bucket (clear disposable zeta-cell) was utilized at 25°C . The instrument measures electrophoretic light scattering of a 35 mW solid state laser beam at a 660 nm wavelength. Smoluchowski's approximation was used to convert the electrophoretic mobility into zeta potential value (Sze et al. 2003). The BCN solutions were prepared in triplicate at concentrations of 1 mg mL^{-1} . All samples were stabilized inside the device for 30 s, and 100 measurements were collected with confidence intervals of 95 % for each sample with standard error of 1.00 mV.

Atomic force microscopy

Aqueous dispersions of BCN and of BCN coated with XG were diluted to $125\text{ }\mu\text{g mL}^{-1}$ and spin-coated on a freshly cleaved mica surface. The dimensions of the isolated BCN before and after XG adsorption were determined by means of atomic force microscopy (AFM) images obtained in the air in the intermittent

contact mode with an Agilent 5500 microscope (Agilent Technologies, Santa Clara, CA, USA), using Mikromasch NSC14 silicon tips (Mikromasch USA, San Jose, CA, USA) with a nominal spring constant of 5.7 N m^{-1} and a resonance frequency of $\sim 100\text{ kHz}$. The scanning areas were $2.0\text{ }\mu\text{m} \times 2.0\text{ }\mu\text{m}$, $4.0\text{ }\mu\text{m} \times 4.0\text{ }\mu\text{m}$ and $8.0\text{ }\mu\text{m} \times 8.0\text{ }\mu\text{m}$. The images were acquired using Pico Image software (Agilent Technologies, Santa Clara, CA, USA) and were processed with the Gwyddion software (Czech Metrology Institute). The root mean square values for surface roughness (rms values), height and width were determined with the Gwyddion software (Czech Metrology Institute). The dimensions of BCN and of XG coated BCN were compared using Student's *t* test by assuming a significant difference if $p \leq 0.01$. Absolute length measurements by AFM are not reliable due to lateral enlargement caused by tip convolution (Yang et al. 2001). However, the height measurements are reliable, so they can be used to estimate the thickness of XG coating on BCN.

The adsorptions of XG on BCN by the LbL technique were determined by the dipping deposition method with a rinsing step between each polymer deposition step. First the substrate surface was modified by spin-coating (2 min at 3000 rpm) PEI solution (1 mg mL^{-1}) on the freshly cleaved mica surface. Under the same conditions, BCN and XG solutions (1 mg mL^{-1}) were deposited alternately. AFM images of the PEI, BCN and XG layers were subsequently obtained in a liquid cell with ultrapure water in tapping mode with an oscillation frequency of $\sim 100\text{ kHz}$.

For the determination of the film thickness scratches were done on the film surface using a clean sharp blade and the residues were removed under a stream of N_2 (Blachechen et al. 2012). The AFM images were taken under an air atmosphere. Then the peak-to-valley distances were measured by means of the Gwyddion software, as shown in the supplementary material (SM4 and SM5).

Adsorption of XG on BCN analyzed in a real time by a quartz crystal microbalance

The adsorption of the XG on BCN was verified through QCM (SRS, Stanford research systems). AT-cut platinum crystal quartz of 5 MHz coated with titanium were cleaned in a piranha solution composed

of $\text{H}_2\text{O}:\text{NH}_4:\text{H}_2\text{O}_2$ (7:1:1, v:v) for 30 min in order to produce a anionic TiO_2 surface and rinsed with deionized water and vacuum dried in an oven. The substrate surface was produced on a TiO_2 quartz surface by depositing 1 mL of polycationic PEI solution (1 mg mL^{-1}) by 15 min followed by spin coating (40 s—10,000 rpm) as described by (Jean et al. 2008; Kolasińska and Warszyński 2005) followed by a similar process for the all BCN samples layer (1 mg mL^{-1}). Real-time QCM experiments were performed in a flow cell (SRS) connected to a syringe pump with a $100 \mu\text{L mL}^{-1}$ flow rate. The BCN and XG solutions (1 mg mL^{-1}) were injected separately, and the sample on the substrate was immediately rinsed with ultrapure water between each deposition of the biopolymer solutions.

Layer by layer deposition and ellipsometry

The alternated deposition of BCN and XG onto PEI coated Si/SiO_2 wafers ($1 \text{ cm} \times 1 \text{ cm}$) was done following the LbL technique. The Si/SiO_2 wafers were immersed in a mixture of NH_4OH (25 % in volume), H_2O_2 (30 % in volume), and distilled water in the volume ratio of 1:1:5 and at the temperature of 70°C during 20 min. Afterwards, the wafers were washed with distilled water and dried by a stream of N_2 . The Si wafers were modified by depositing 1 mL of polycationic PEI solution (1 mg mL^{-1}) by 15 min followed by spin coating (40 s, 10,000 rpm) (Jean et al. 2008; Kolasińska and Warszyński 2005) followed by a similar process for the all BCN samples layer (1 mg mL^{-1}). The next layers were deposited by dipping in a XG or BCN solutions (1 mg mL^{-1}) for 15 min, with rinsed process with ultrapure water between each deposition.

Ellipsometric measurements were performed in air using a vertical computer-controlled DRE-EL02 ellipsometer (Ratzeburg, Germany) (Kosaka et al. 2005). The angle of incidence was set at 70.0° and the wavelength, λ , of the He–Ne laser was 632.8 nm. A multilayer model composed of the substrate, the unknown layer and the surrounding medium was used for data interpretation. The thickness, d_x and the refractive index, n_x , of the unknown layer were calculated from the ellipsometric angles, Δ and Ψ , using the fundamental ellipsometric equation and iterative calculations with Jones matrices (Azzam and Bashara 1987):

$$e^{i\Delta} \tan \Psi = \frac{R_p}{R_s} = (n_x, d_x, \lambda, \phi) \quad (7)$$

where R_p and R_s are the overall reflection coefficients for the parallel and perpendicular waves, respectively. These coefficients are functions of the angle of incidence, ϕ ; the wavelength, λ ; the radiation; and the refractive index and thickness of each layer of the model, which are n_x and d_x , respectively.

From the ellipsometric angles, Δ and Ψ and a multilayer model composed of silicon, silicon dioxide, the polysaccharide layer and air, it was possible to determine only the thickness of the polysaccharide layer. The thickness of the silicon dioxide layers was determined in air by assuming a refractive index of $3.88-0.018i$ and an infinite thickness for silicon (Palik 1985). The refractive index for the surrounding medium (air) was taken as 1.00. Because the native silicon dioxide layer was notably thin, its refractive index was taken to be 1.462 (Palik 1985). The mean thickness of the native silicon dioxide layer was $2.0 \pm 0.2 \text{ nm}$. After determining the thickness of the silicon dioxide layer, the mean thicknesses of the adsorbed PEI, BCN and XG layers were determined in air by ellipsometry, considering the refractive index of PEI as 1.46 (Izquierdo et al. 2005), BCN as 1.60 (Nogi and Yano 2008) and XG as 1.50.

Contact angle

Contact angle (CA) measurements (DataPhysics OCA 15 Plus tensiometer, Filderstadt, Germany) were performed for spin-coated films on Si/SiO_2 wafers, using the sessile drop method with MilliQ water droplets of $3 \mu\text{L}$. All measurements were conducted at 25°C . The CA calculations were performed with SCA 20 DataPhysics software (Filderstadt, Germany). Each CA value was the average of at least three drops of liquid per surface.

Results and discussion

Characterization of bacterial cellulose pulp and xyloglucan

The dried BC membrane pieces were initially dispersed in ultrapure water, milled and submitted to ultrasound treatment, resulting in a BC fiber pulp suspension. These processes were necessary to increase the surface

area and to enable effective acid hydrolysis. AFM topographic images (SM1) revealed particle size distributions ranging from 10 to 100 nm in diameter of the fibers.

Characterization of bacterial cellulose nanocrystals

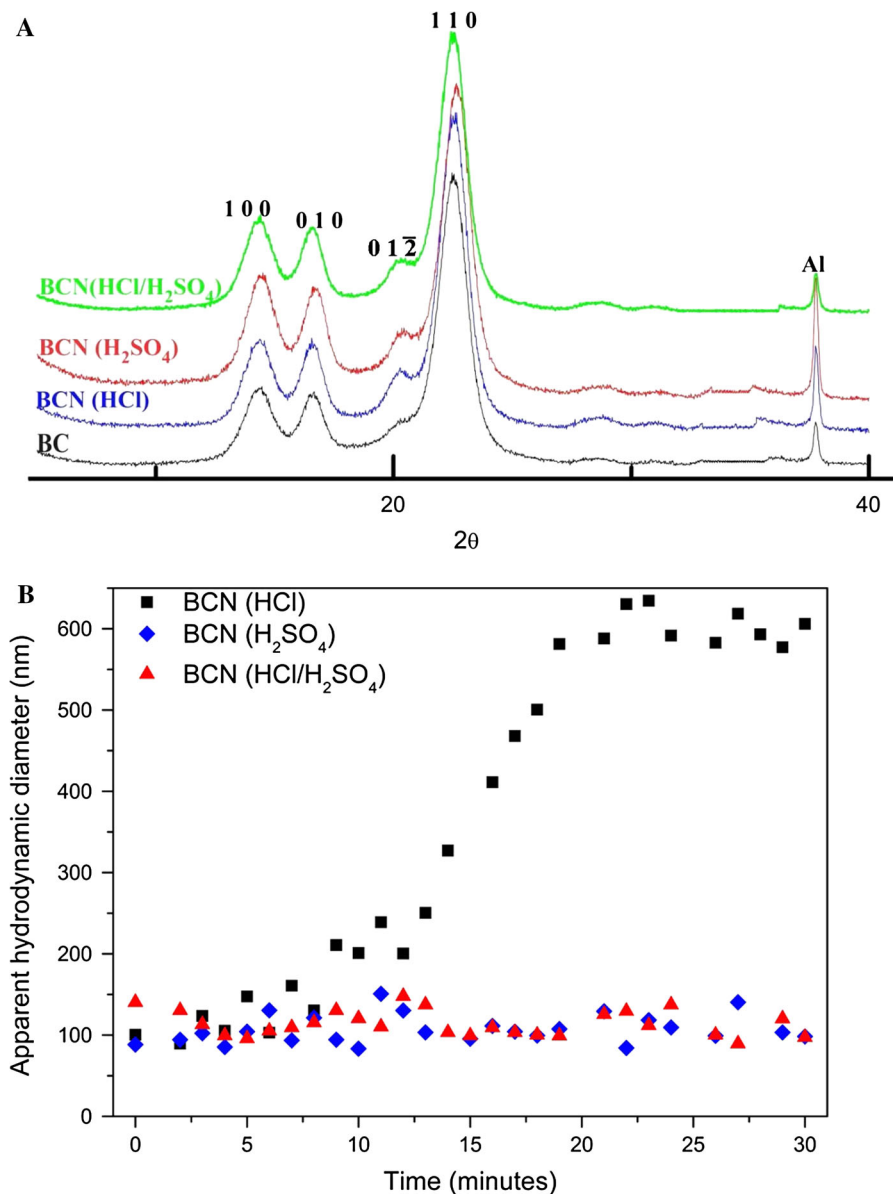
Bacterial cellulose nanocrystals (BCN) were produced from pulp by acid hydrolysis using three distinct media, namely, HCl, H₂SO₄ and a mixture of HCl and H₂SO₄, to generate BCN with distinct sulfate esterification levels in a single-step procedure. H₂SO₄ cellulose hydrolysis followed by acid-catalyzed or solvolytic desulfation were other tentative ways, but not efficient, to remove sulfate groups from cellulose nanocrystals surface (Gu et al. 2013). All isolated BCN presented similar crystallinity, morphology and size distribution. According to compared diffraction patterns obtained from crystal information file (.cif) (French 2014), the patterns were indexed according to cellulose I α indexation as described by Sugiyama et al. (1991). The peaks used for crystallinity calculations were 1 0 0, 0 1 0, 0 1 2 and 1 1 0 crystallographic planes, assigned to diffraction angles of 14.4°, 16.7°, 20.5° and 22.7°, respectively (Fig. 1a). The contribution of the peak at 37.7° of 2 θ was attributed to the aluminum sample holder and was not used for calculations of crystallinity. As expected, the pretreatment (mill and ultrasound) and the hydrolysis of BC caused no alteration in the crystallinity pattern (I α), as observed in the XRD pattern. The crystalline peaks and d-spaces also did not differ between the samples (Table 1). All BCN samples presented larger *CrI*, when hydrolyzed with HCl (83 %), H₂SO₄ (82 %) and HCl/H₂SO₄ (82 %) than that observed for pristine BC (72 %), in agreement to the results obtained by Martínez-Sanz et al. (2011). Such increase in *CrI* corresponds to the decrease in the cellulose amorphous region after hydrolysis. As shown by the apparent crystalline size (ACS) values determined for BCN samples, the hydrolysis processes were specific to the amorphous regions, as revealed by no significant difference in the crystal sizes after the process. AFM topographic images (SM2 to SM4) exhibited the typical whisker aspect ratio with similar size dimensions (Araki et al. 1998; Battista 1950; Souza Lima and Borsali 2004).

In contrast, the hydrolytic processes produced BCN with different mean sulfate contents in the range of 0–0.65 % (standard deviation of 0.01) (Table 1). The quantification of cellulose nanowhiskers' sulfate esterification levels was analyzed by elemental analysis because this technique is one of the most sensitive and reliable to measure sulfate content (Gu et al. 2013). Other techniques to quantify sulfate, such as conductometric titration, could lead to underestimation of sulfate content, since there are sulfate groups inaccessible to titrants (Araki et al. 1998; Dong et al. 1998; Gu et al. 2013). Despite the relatively low sulfate degree produced by this process when compared with the cellulose total mass, those values represent large functionalization concerning the material's surface, as already described by Lin and Dufresne (2014b). Indeed, these small sulfate content differences between BCN resulted in distinct colloidal behaviors. As expected, BCN-HCl presented low surface charge, evidenced by ζ -potential value of $-(5 \pm 1)$ mV, which caused poor colloidal stability. As evidenced in Fig. 1b, mean particle size increased continuously as a function of time, due to aggregation. In such situation, the low electrostatic repulsion is overcome by hydrogen bonds and attractive van der Waals forces (Araki et al. 1998; Jó et al. 2010; Marchessault et al. 1959; Winter et al. 2010). On the other hand, BCN-H₂SO₄ or BCN-HCl/H₂SO₄ exhibited ζ -potential values of $-(40 \pm 1)$ mV and $-(46 \pm 1)$ mV, respectively, due to the introduction of sulfate groups on the surface. The corresponding mean particle sizes remained practically constant as a function of time (Fig. 1b), indicating that the electrostatic repulsion among the OSO₃[−] groups on BCN avoided aggregation, keeping the colloidal systems stable. The colloidal stability of sulfated cellulose nanocrystals dispersed in water requires minimum ζ -potential value of $-(25)$ mV in order to produce effective electrostatic repulsion among the particles, and an increase in OSO₃[−] content is not able to cause a substantial difference (Lin and Dufresne (2014b); Winter et al. (2010). In fact, the increase in the sulfate content from 0.42 ± 0.01 to 0.65 ± 0.01 caused a change of 6 mV in the ζ -potential values.

Influence of BCN sulfate content on xyloglucan adsorption

In order to investigate the adsorption behavior of XG on BCN samples, XG solutions were prepared in the

Fig. 1 **a** X-ray diffractograms obtained for the BC and BCN samples. **b** Apparent hydrodynamic diameter determined for BCN samples as a function of time



diluted range or below its c^* ($<1.38 \text{ mg mL}^{-1}$) (Jó et al. 2010). In the more concentrated range, XG aggregation leads to chain entanglement, resulting in a more disordered and unstable layer adsorbed onto BCN, as previously observed by Cerclier et al. (2010).

The BCN samples with different amounts of sulfate groups produced by a single modification step were used as substrates for the adsorption of XG from solution. Nevertheless, it is complicated to compare XG adsorption to BCN particles with distinct colloidal behavior, because BCN-HCl

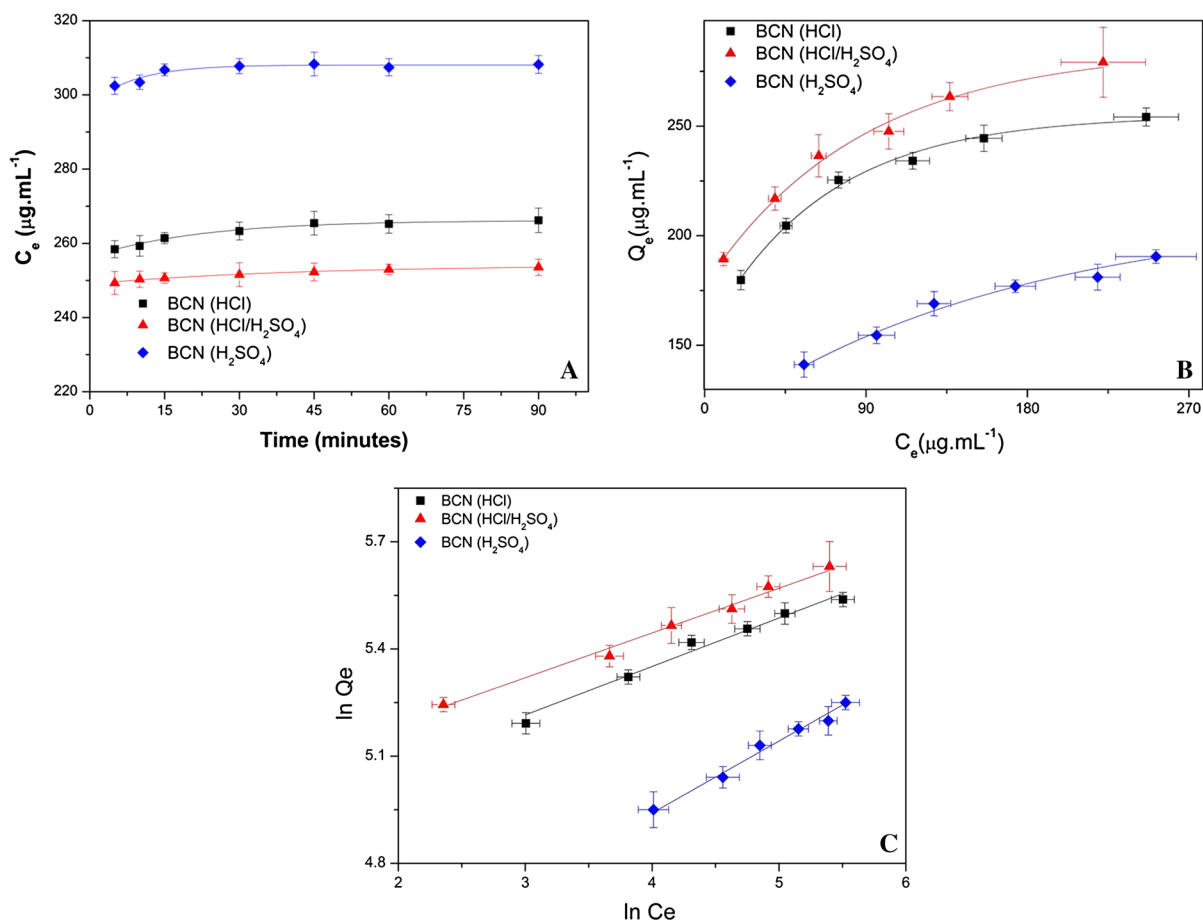
aggregation results in larger BCN particles with lower surface area than the BCN-HCl/H₂SO₄ or BCN-H₂SO₄ particles, as shown in Fig. 1b. Thus, in order to analyze XG adsorption on dispersed BCN particles, all samples were submitted to brief sonication (see dynamic light scattering analysis in “Materials and methods” section).

The effect of adsorption time on the adsorbed amount of XG onto BCN (Q_e values) was investigated for XG at $500 \mu\text{g mL}^{-1}$ and BCN at 1 mg mL^{-1} , at $(25 \pm 1)^\circ\text{C}$, as a function of time, as shown in Fig. 2a.

Table 1 Zeta (ζ) potential, sulfur content and x-ray diffraction analysis of pretreated bacterial cellulose pulp (BC) and cellulose nanocrystals (BCN) obtained by different processes (HCl, H₂SO₄ and HCl/H₂SO₄)

Sample	ζ (–mV)	S (% w/w)	CrI (%)	1 0 0 ACS/d (nm)	0 1 0 ACS/d (nm)	1 1 0 ACS/d (nm)
BC	n.d	n.d	72	5.63/0.60	7.49/0.53	5.83/0.39
BCN-HCl	5 ± 1	0	83	5.41/0.60	7.21/0.53	5.42/0.39
BCN-HCl/H ₂ SO ₄	40 ± 1	0.42	82	5.54/0.60	7.94/0.53	5.32/0.39
BCN-H ₂ SO ₄	46 ± 1	0.65	82	5.50/0.60	7.33/0.53	5.22/0.39

ζ zeta potential, *S* sulfur content, *CrI* crystallinity index; *n.d* not determined, ACS apparent crystalline size. See XRPD method, *d* interplanar distances

**Fig. 2** **a** Amount of XG unbound to BCN quantified in the supernatant (C_e) after centrifugation as a function of time. **b** Adsorption isotherms for adsorption of XG onto BCN. **c** Linearized Freundlich fitting of the adsorption isotherms

Regardless the BCN type, adsorption equilibrium was achieved after 5 min, corroborating the XG-cellulose adsorption behavior observed by Lima and Buckridge (2001). Desorption processes were negligible, in agreement with previous findings that XG

adsorption to cellulose is a quasi-irreversible process (Bodin et al. 2007; Karaaslan et al. 2011; Kummerer et al. 2011; Lima and Buckridge 2001; Lima et al. 2004; Shirakawa et al. 1998; Zhou et al. 2007; Zykawska et al. 2008).

Adsorption isotherms were determined for XG on BCN (1 mg mL^{-1}) with incubation period of 30 min at $(25 \pm 1)^\circ\text{C}$. It was only possible to evaluate adsorption using XG concentrations higher than $200 \mu\text{g mL}^{-1}$ (this value corresponds to the initial XG concentration before adsorption onto BCN). Below this concentration, no XG chains could be detected in the supernatant (C_e), indicating that all XG chains were adsorbed on the BCN surface (the I_2/KI method's lower limit detection is $5 \mu\text{g mL}^{-1}$). On the other hand, in the XG concentration range from 200 to $500 \mu\text{g mL}^{-1}$, different adsorption profiles were achieved (Fig. 2b).

Although the Langmuir model is frequently applied to fit the adsorption of XG onto cellulose nanocrystals (Cerclier et al. 2010; Dammak et al. 2015; Gu and Catchmark 2013; Hayashi et al. 1994; Lopez et al. 2010; Zykwiniska et al. 2008), it was inadequate for the present study due to the irreversible adsorption and heterogeneous substrates. The Langmuir adsorption model considers that the process is reversible, all binding sites have the same energy and monolayer formation on the substrate. It is well known that: (1) XG adsorption onto cellulose is quasi-irreversible (Bodin et al. 2007; Karaaslan et al. 2011; Kummerer et al. 2011; Lima and Buckeridge 2001; Lima et al. 2004; Shirakawa et al. 1998; Zhou et al. 2007; Zykwiniska et al. 2008); (2) there are at least two different binding affinities due the presence of hydrophilic and hydrophobic regions on cellulose surfaces (Hanus and Mazeau 2006; Zhao et al. 2014; Zykwiniska et al. 2008); and (3) adsorption can take place in a multilayer arrangement (Cerclier et al. 2010; Jean et al. 2009; Winter et al. 2010).

Therefore, instead of the Langmuir adsorption model, we chose the Freundlich empirical adsorption model to fit the experimental data, mainly because the reversible adsorption and homogeneous substrate premises are not required. Moreover, the Freundlich model seems more appropriate to describe the binding data of XG to BCN because it considers different types of binding sites and binding affinity. Indeed, Zykwiniska et al. (2008) compared both Langmuir and Freundlich models for XG adsorption onto microcrystalline cellulose and concluded that Freundlich was more appropriate to describe XG-cellulose interactions. Thus, in the present work the adsorption isotherms of XG onto BCN with different OSO_3^- contents were fitted with the Freundlich model, Eq. 5 (Fig. 2c), yielding the fit

Table 2 Fitting parameters of Freundlich adsorption isotherm model determined for the adsorption of xyloglucan (XG) on bacterial cellulose nanoparticles (BCN) isolated by use of HCl (BCN-HCl), a mix of HCl and H_2SO_4 (BCN-HCl/ H_2SO_4) and H_2SO_4 (BCN- H_2SO_4)

Sample	m	$1/n$	Height (nm)
BCN-HCl	–	–	* 8.98 ± 1.7
+XG	4.75 ± 0.05	0.12 ± 0.01	* 14.2 ± 2.1
BCN-HCl/ H_2SO_4	–	–	* 8.9 ± 2.2
+XG	4.98 ± 0.07	0.15 ± 0.01	* 13.9 ± 2.9
BCN- H_2SO_4	–	–	* 9.21 ± 2.6
+XG	4.12 ± 0.10	0.20 ± 0.01	* 15.2 ± 2.1

Mean nanoparticle height determined by atomic force microscopy measurements

* ($p < 0.01$) statistical difference between height of BCN before and after XG adsorption

parameters complex function (m) and heterogeneity index ($1/n$), as presented in Table 2.

The m values, which are related to the average binding affinity and maximal adsorption capacity, determined for XG on BCN with 0.42 % OSO_3^- (BCN-HCl/ H_2SO_4) were the largest, followed by that for XG on BCN without OSO_3^- (BCN-HCl). The smallest m value was determined for XG on BCN with 0.65 % OSO_3^- (BCN- H_2SO_4). The $1/n$ parameters correlated directly with the sulfate content in BCN; the highest was the OSO_3^- content, the largest was the surface heterogeneity ($1/n$ value). These findings allow proposing that the OSO_3^- introduction on BCN surface to some extent (0.42 %) was beneficial because it avoided aggregation (Fig. 1b) and kept the available surface area large. However, upon increasing the sulfate content to 0.65 %, the surface area available was still very large, but the surface heterogeneity was enhanced. The substrate heterogeneity might affect the original complementarities between OH groups of the native glycosidic backbones, which are known to play a main role in interaction between cellulose and XG (Levy et al. 1991; Morris et al. 2004). We summarized these two effects of BCN sulfur content on adsorption to XG in Fig. 3.

Dispersions of XG coated BCN were deposited onto Si wafers, dried and analyzed by AFM. They presented similar morphology (figure not shown). After XG adsorption, all BCN samples presented increase in height of $5.4 \pm 0.4 \text{ nm}$, suggesting that the XG adsorbed chains adopted the BCN-like

conformation (Table 2), corroborating literature reports about XG–cellulose interactions (Levy et al. 1991; Ogawa et al. 1990; Souza et al. 2013; Taylor and Atkins 1985; Whitney et al. 1995). The dimensions were measured only for isolated particles, since it was difficult to evaluate aggregated particles in solution from those aggregated during the drying process.

The adsorption behavior of XG on thin films of BCN was also investigated. The BCN layers were deposited onto flat ($\text{rms} = 0.7 \pm 0.3 \text{ nm}$) spin-coated PEI layers ($1.5 \pm 0.4 \text{ nm}$) thick. PEI layers are well suited to obtain uniform coatings and subsequent multilayer buildup (Jean et al. 2008; Kolasińska and Warszyński 2005). The thickness of the first BCN layer was ($10 \pm 1 \text{ nm}$), regardless the sulfate content, as shown in Fig. 4a and Table 1-SM (Supplementary Material). However, the BCN-HCl layer presented a

smaller rms value ($5.1 \pm 1.3 \text{ nm}$) than sulfated BCN layers ($\sim 8 \text{ nm}$), indicating better packing of uncharged BCN on the PEI surface. The PEI layer presented contact angle of $(69 \pm 1)^\circ$ for water. After the first deposition of BCN-HCl/ H_2SO_4 or BCN- H_2SO_4 layers, the mean contact angle value decreased to $(22.0 \pm 0.4)^\circ$ due to the high hydrophilic OSO_3^- charged surface, whereas in the case of the BCN-HCl layer it decreased to $(43.0 \pm 0.9)^\circ$.

The next alternated depositions were made with XG and BCN suspensions under constant flux in the QCM cell. Figure 4b shows the frequency shift (Δf) determined after each deposition. The 1st XG deposition onto BCN-HCl surface caused the largest change in Δf , corresponding to the largest XG mass deposition. The smallest change in Δf values was observed for the deposition onto BCN-HCl/ H_2SO_4 layer, corroborating with the adsorption behavior observed in dispersions, suggesting that introduction of OSO_3^- disturbs the original cellulose-XG interaction. The first deposited XG layer onto sulfated BCN layers changed the contact angle to $(42 \pm 1)^\circ$, indicating less amount of charges exposed to the medium due to the XG coverage. The XG coated BCN-HCl layer presented contact angle of $(34.0 \pm 0.7)^\circ$, revealing that XG layer is more hydrophilic than uncharged BCN. On the other hand, the mean thickness values of the XG layer amounted to $(14 \pm 1 \text{ nm})$, regardless the type of BCN layer. The second BCN-HCl layer presented irregular coverage (Figure SM4), larges changes in Δf and mean thickness values. The films' thickness in this case were evaluated also by atomic force microscopy (see the section on “Atomic force microscopy” in the “Materials and methods” for more details) in order to confirm the large increase in thickness by ellipsometry (Blachechen et al. 2012). Although this measurement is not as accurate as ellipsometry, the height difference between the film surface and substrate after film scratching (peak-to-valley distance) provides an estimate of the thickness. The mean peak-to-valley distance was up to 200 nm (see SM5). The large thickness and irregular film deposition is due to BCN-HCl aggregation. The BCN-HCl suspension already contained aggregated particles before adsorbing on the surface, as shown by the dynamic light scattering profiles. Furthermore, a BCN-HCl covered surface is attractive for continuous adsorption of other BCN particles or aggregates in a constant flux of BCN suspension. These results are in accordance with

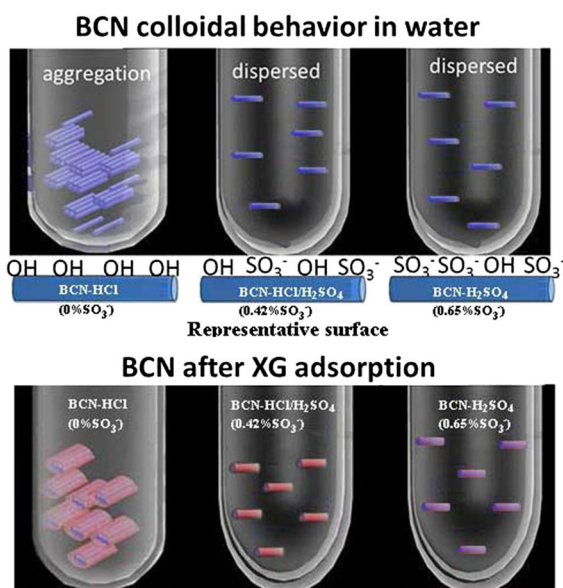


Fig. 3 Schematic representation of XG adsorption on BCN-HCl, BCN-HCl/ H_2SO_4 and BCN- H_2SO_4 . In the picture, the BCN are represented by *blue rectangles* and XG is represented by *red lines*. The *upper one* demonstrates the colloidal behavior of BCN in water (at the *bottom* of the picture there is a representation of the BCN surface related to the sulfate content), and the *lower one* after XG adsorption. After XG adsorption, the BCN-HCl results in lower XG mass due to the lower surface area of aggregated BCN particles. On the other hand, the BNC-HCl/ H_2SO_4 and BCN- H_2SO_4 adsorbed XG on dispersed BCN particles (with higher surface area due to the electrostatic repulsion of SO_3^- groups). However, the BCN- H_2SO_4 presented lower XG adsorbed, probably due to the high sulfate content (0.65 % SO_3^-). (Color figure online)

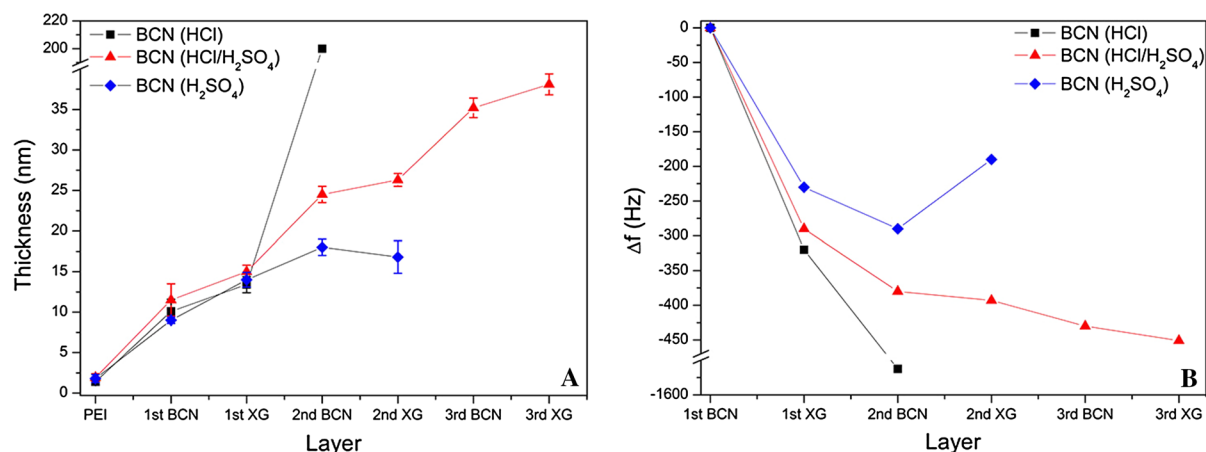


Fig. 4 **a** Evolution of thickness (by ellipsometry) and **b** (Δf) (by quartz crystal microbalance), of alternated layers of bacterial cellulose nanocrystals (BCN) and xyloglucan (XG)

Winter et al. (2010), who demonstrated that BCN-HCl aggregation results in irregular film deposition and high thickness. Thus, the deposition of next layers of BCN-HCl was interrupted.

The second layer of BCN-HCl/H₂SO₄ was thicker (24 ± 1 nm) than the 2nd deposited layer of BCN-H₂SO₄ (18 ± 1 nm). The adsorption of BCN-HCl/H₂SO₄ caused larger change in Δf (-380 Hz), which corresponds to larger mass deposition, than the adsorption of BCN-H₂SO₄ (-290 Hz). The lower mass deposition and thinner layer of BCN-H₂SO₄ resulted from the higher charge density, which promoted electrostatic repulsion and avoided the adsorption of more BCN particles. On the other hand, the BCN-HCl presented a constant increase of adsorption due to aggregation.

The second deposition of XG layer on the BCN-H₂SO₄ layer after 5 min of XG flushing and followed by water washing resulted in desorption, as revealed by the decrease of the resonance frequency (Δf) and decrease of the thickness of the previous BCN layer measured by ellipsometry. Further attempts by adding more XG solution resulted in the pronounced decrease of Δf , indicating new desorption process. On the contrary, the 2nd deposition of XG layer on the BCN-HCl/H₂SO₄ surface led to an increase in thickness (26 ± 1 nm) similar to first deposition of XG layer, with no desorption process. Additional alternate depositions of BCN and XG presented similar increase in thickness and mass quantity. Comparing the LbL

deposition involving BCN-HCl/H₂SO₄ and BCN-H₂SO₄, the latter yielded less stable layers due to the increase of surface sulfate content.

The high affinity between cellulose and XG has a well-known quasi-irreversible adsorption at room temperature (25 °C). This is mainly due to the high content of hydrogen bonds (cellulose-OH-OH-XG). Our results demonstrate that the sulfate groups content on the surface of BCN as large as 0.65 % can reduce the adsorption of XG. However, through better control of the reaction conditions during isolation of the BCN, it is possible to isolate BCN with a lower degree of OSO_3^- , without significantly impairing the original adsorption with XG, preserving the advantages of high colloidal stability of the particles caused by the introduction of sulfate groups. These findings could be usefully for development of BCN-XG nanoparticles and multilayer nanofilms with better adsorption stability (no desorption) and high thermal stability (due the lower OSO_3^- introduction). Although individual BCN particles and BCN nanofilms are already promising in different fields (e.g., biosensors, enzyme supports, biomedical devices, thermoplastic reinforcement, drug release, hydrogels, pickering emulsions) (Blachechen et al. 2013), the coverage by XG could improve these properties even more and/or extend the application field. The modification of BCN interfacial properties with XG could be an easy way to form galactose functionalized particles that could be used as a drug delivery agent in liver cancer, for example. The combination of XG and BCN is advantageous

compared to using them individually. It is more difficult to functionalize BC, and it is more difficult to obtain well-defined and stable nanoparticles of XG.

Conclusions

Sulfate esterification reaction during the isolation of cellulose crystals, by use of H_2SO_4 modifies the adsorption between cellulose nanocrystals and XG in aqueous media. Using three distinct sulfate contents on cellulose nanocrystal surfaces (0, 0.42 and 0.65 %), we demonstrated that 0.42 % prevents particle aggregation and also does not significantly impair the adsorption to XG. Besides this, the 0.42 % concentration produces better coverage composed of more homogeneous and intercalated layers of cellulose nanocrystals and XG (without desorption) than concentrations of 0 and 0.65 %. Although the results presented here demonstrate clear adsorption difference caused by OSO_3^- esterification, more investigation is necessary to clarify what causes this different interaction between the BCN and XG interfaces (studies are under progress and will be reported in a future article).

Acknowledgments We acknowledge the Brazilian funding agencies CNPq (Conselho Nacional de Pesquisa), Rede Nanobiotec/Capes-Brazil and the REUNI program for financial support. We are grateful to Dr. Fernando Wypych and Dr. Fábio da Silva Lisboa for XRPD analysis, to Dr. Graciela B. Muniz (DEF, UFPR) for access to the supermass colloid mill, to Dr. Lionel Gamarra (Instituto Cérebro, Hospital Albert Einstein) for ζ -potential experiments, to Membrane® (bacterial cellulose sample sheets) and Balasanka Mills (XG) for sample donations.

References

- Araki J, Wada M, Kuga S, Okano T (1998) Flow properties of microcrystalline cellulose suspension prepared by acid treatment of native cellulose. *Colloids Surf A* 142:75–82. doi:[10.1016/S0927-7757\(98\)00404-X](https://doi.org/10.1016/S0927-7757(98)00404-X)
- Azzam RMA, Bashara NM (1987) Ellipsometry and polarized light. North Holland, Amsterdam
- Battista OA (1950) Hydrolysis and crystallization of cellulose. *Ind Eng Chem* 42:502–507. doi:[10.1021/ie50483a029](https://doi.org/10.1021/ie50483a029)
- Ben Azouz K, Ramires EC, van den Fonteyne W, El Kissi N, Dufresne A (2011) Simple method for the melt extrusion of a cellulose nanocrystal reinforced hydrophobic polymer. *ACS Macro Lett* 1:236–240. doi:[10.1021/mz2001737](https://doi.org/10.1021/mz2001737)
- Berne BJ, Pecora R (2000) Dynamic light scattering: with applications to chemistry, biology, and physics. Dover Publications, Inc., New York
- Blachechen L, Souza M, Petri DS (2012) Effect of humidity and solvent vapor phase on cellulose esters films. *Cellulose* 19:443–457. doi:[10.1007/s10570-012-9654-z](https://doi.org/10.1007/s10570-012-9654-z)
- Blachechen L, de Mesquita J, de Paula E, Pereira F, Petri DS (2013) Interplay of colloidal stability of cellulose nanocrystals and their dispersibility in cellulose acetate butyrate matrix. *Cellulose* 20:1329–1342. doi:[10.1007/s10570-013-9881-y](https://doi.org/10.1007/s10570-013-9881-y)
- Bodin A, Ahrenstedt L, Fink H, Brumer H, Risberg B, Gatenholm P (2007) Modification of nanocellulose with a xyloglucan—RGD conjugate enhances adhesion and proliferation of endothelial cells: implications for tissue engineering. *Biomacromolecules* 8:3697–3704. doi:[10.1021/bm070343q](https://doi.org/10.1021/bm070343q)
- Bondeson D, Mathew A, Oksman K (2006) Optimization of the isolation of nanocrystals from microcrystalline cellulose by acid hydrolysis. *Cellulose* 13:171–180. doi:[10.1007/s10570-006-9061-4](https://doi.org/10.1007/s10570-006-9061-4)
- Carpita NC, Gibeault DM (1993) Structural models of primary cell walls in flowering plants: consistency of molecular structure with the physical properties of the walls during growth. *Plant J* 3:1–30. doi:[10.1111/j.1365-3113X.1993.tb00007.x](https://doi.org/10.1111/j.1365-3113X.1993.tb00007.x)
- Cerclier C, Cousin F, Bizot H, Moreau C, Cathala B (2010) Elaboration of spin-coated cellulose–xyloglucan multilayered thin films. *Langmuir* 26:17248–17255. doi:[10.1021/la102614b](https://doi.org/10.1021/la102614b)
- Chen Y, Stipanovic A, Winter W, Wilson D, Kim Y-J (2007) Effect of digestion by pure cellulases on crystallinity and average chain length for bacterial and microcrystalline celluloses. *Cellulose* 14:283–293. doi:[10.1007/s10570-007-9115-2](https://doi.org/10.1007/s10570-007-9115-2)
- Dammak A et al (2015) Exploring architecture of xyloglucan cellulose nanocrystal complexes through enzyme susceptibility at different adsorption regimes. *Biomacromolecules* 16:589–596. doi:[10.1021/bm5016317](https://doi.org/10.1021/bm5016317)
- Doliška A, Willför S, Strnad S, Ribitsch V, Kleinschek KS, Eklund P, Xu C (2012) Antithrombotic properties of sulfated wood-derived galactoglucomannans. *Holzforschung* 66:149. doi:[10.1515/HF.2011.136](https://doi.org/10.1515/HF.2011.136)
- Dong X, Revol J-F, Gray D (1998) Effect of microcrystallite preparation conditions on the formation of colloid crystals of cellulose. *Cellulose* 5:19–32. doi:[10.1023/A:1009260511939](https://doi.org/10.1023/A:1009260511939)
- Eronen P, Österberg M, Heikkinen S, Tenkanen M, Laine J (2011) Interactions of structurally different hemicelluloses with nanofibrillar cellulose. *Carbohydr Polym* 86:1281–1290. doi:[10.1016/j.carbpol.2011.06.031](https://doi.org/10.1016/j.carbpol.2011.06.031)
- Filson PB, Dawson-Andoh BE, Schwegler-Berry D (2009) Enzymatic-mediated production of cellulose nanocrystals from recycled pulp. *Green Chem* 11:1808–1814
- Freitas RA, Martin S, Santos GL, Valenga F, Buckeridge MS, Reicher F, Sierakowski MR (2005) Physico-chemical properties of seed xyloglucans from different sources. *Carbohydr Polym* 60:507–514. doi:[10.1016/j.carbpol.2005.03.003](https://doi.org/10.1016/j.carbpol.2005.03.003)
- French A (2014) Idealized powder diffraction patterns for cellulose polymorphs. *Cellulose* 21:885–896. doi:[10.1007/s10570-013-0030-4](https://doi.org/10.1007/s10570-013-0030-4)

- Fry SC (1989) The structure and functions of xyloglucan. *J Exp Bot* 40:1–11. doi:[10.1093/jxb/40.1.1](https://doi.org/10.1093/jxb/40.1.1)
- Gu J, Catchmark J (2013) The impact of cellulose structure on binding interactions with hemicellulose and pectin. *Cellulose* 20:1613–1627. doi:[10.1007/s10570-013-9965-8](https://doi.org/10.1007/s10570-013-9965-8)
- Gu J, Catchmark JM, Kaiser EQ, Archibald DD (2013) Quantification of cellulose nanowhiskers sulfate esterification levels. *Carbohydr Polym* 92:1809–1816. doi:[10.1016/j.carbpol.2012.10.078](https://doi.org/10.1016/j.carbpol.2012.10.078)
- Hantus S, Pauly M, Darvill AG, Albersheim P, York WS (1997) Structural characterization of novel L-galactose-containing oligosaccharide subunits of jojoba seed xyloglucans. *Carbohydr Res* 304:11–20
- Hanus J, Mazeau K (2006) The xyloglucan–cellulose assembly at the atomic scale. *Biopolymers* 82:59–73. doi:[10.1002/bip.20460](https://doi.org/10.1002/bip.20460)
- Hayashi T (1989) Xyloglucans in the primary cell wall. *Annu Rev Plant Physiol Plant Mol Biol* 40:139–168. doi:[10.1146/annurev.pp.40.060189.001035](https://doi.org/10.1146/annurev.pp.40.060189.001035)
- Hayashi T, Ogawa K, Mitsuishi Y (1994) Characterization of the adsorption of xyloglucan to cellulose. *Plant Cell Physiol* 35:1199–1205
- Hermans PH (1946) Deformation mechanism of cellulose gels. I. Present status of the problem. *J Polym Sci* 1:389–392. doi:[10.1002/pol.1946.120010506](https://doi.org/10.1002/pol.1946.120010506)
- Hsieh YC, Yano H, Nogi M, Eichhorn SJ (2008) An estimation of the Young's modulus of bacterial cellulose filaments. *Cellulose* 15:507–513. doi:[10.1007/s10570-008-9206-8](https://doi.org/10.1007/s10570-008-9206-8)
- Iguchi M, Yamanaka S, Budhiono A (2000) Bacterial cellulose—a masterpiece of nature's arts. *J Mater Sci* 35:261–270. doi:[10.1023/a:1004775229149](https://doi.org/10.1023/a:1004775229149)
- Iler RK (1966) Multilayers of colloidal particles. *J Colloid Interface Sci* 21:569–594. doi:[10.1016/0095-8522\(66\)90018-3](https://doi.org/10.1016/0095-8522(66)90018-3)
- Izquierdo A, Ono SS, Voegel JC, Schaaf P, Decher G (2005) Dipping versus spraying: exploring the deposition conditions for speeding up layer-by-layer assembly. *Langmuir* 21:7558–7567. doi:[10.1021/la047407s](https://doi.org/10.1021/la047407s)
- Jean B, Heux L, Dubreuil F, Chambat G, Cousin F (2008) Non-electrostatic building of biomimetic cellulose–xyloglucan multilayers. *Langmuir* 25:3920–3923. doi:[10.1021/la802801q](https://doi.org/10.1021/la802801q)
- Jean B, Heux L, Dubreuil F, Chambat G, Cousin F (2009) Non-electrostatic building of biomimetic cellulose–xyloglucan multilayers. *Langmuir* 25:3920–3923. doi:[10.1021/la802801q](https://doi.org/10.1021/la802801q)
- Jia Z, Qin Q, Darvill AG, York WS (2003) Structure of the xyloglucan produced by suspension-cultured tomato cells. *Carbohydr Res* 338:1197–1208. doi:[10.1016/S0008-6215\(03\)00079-X](https://doi.org/10.1016/S0008-6215(03)00079-X)
- Jó TA, Petri DFS, Beltramini LM, Lucyszyn N, Sierakowski MR (2010) Xyloglucan nano-aggregates: physico-chemical characterisation in buffer solution and potential application as a carrier for camptothecin, an anti-cancer drug. *Carbohydr Polym* 82:355–362. doi:[10.1016/j.carbpol.2010.04.072](https://doi.org/10.1016/j.carbpol.2010.04.072)
- Kalashnikova I, Bizot H, Cathala B, Capron I (2011) New pickering emulsions stabilized by bacterial cellulose nanocrystals. *Langmuir* 27:7471–7479. doi:[10.1021/la200971f](https://doi.org/10.1021/la200971f)
- Karaaslan MA, Tshabalala MA, Yelle DJ, Buschle-Diller G (2011) Nanoreinforced biocompatible hydrogels from wood hemicelluloses and cellulose whiskers. *Carbohydr Polym* 86:192–201. doi:[10.1016/j.carbpol.2011.04.030](https://doi.org/10.1016/j.carbpol.2011.04.030)
- Kolasińska M, Warszyński P (2005) The effect of nature of polyions and treatment after deposition on wetting characteristics of polyelectrolyte multilayers. *Appl Surf Sci* 252:759–765. doi:[10.1016/j.apsusc.2005.02.060](https://doi.org/10.1016/j.apsusc.2005.02.060)
- Kooiman P (1960) A method for the determination of amyloid in plant seeds. *Recueil des Travaux Chimiques des Pays-Bas* 79:675–678. doi:[10.1002/recl.19600790703](https://doi.org/10.1002/recl.19600790703)
- Kosaka PM, Kawano Y, Salvadori MC, Petri DFS (2005) Characterization of ultrathin films of cellulose esters. *Cellulose* 12:351–359. doi:[10.1007/s10570-005-2205-0](https://doi.org/10.1007/s10570-005-2205-0)
- Kummerer K, Menz J, Schubert T, Thielemans W (2011) Biodegradability of organic nanoparticles in the aqueous environment. *Chemosphere* 82:1387–1392. doi:[10.1016/j.chemosphere.2010.11.069](https://doi.org/10.1016/j.chemosphere.2010.11.069)
- Levy S, York WS, Stuike-Prill R, Meyer B, Staehelin LA (1991) Simulations of the static and dynamic molecular conformations of xyloglucan. The role of the fucosylated side-chain in surface-specific sidechain folding. *Plant J* 1:195–215
- Lima DU, Buckeridge MS (2001) Interaction between cellulose and storage xyloglucans: the influence of the degree of galactosylation. *Carbohydr Polym* 46:157–163. doi:[10.1016/S0144-8617\(00\)00297-6](https://doi.org/10.1016/S0144-8617(00)00297-6)
- Lima DU, Loh W, Buckeridge MS (2004) Xyloglucan–cellulose interaction depends on the sidechains and molecular weight of xyloglucan. *Plant Physiol Biochem* 42:389–394. doi:[10.1016/j.plaphy.2004.03.003](https://doi.org/10.1016/j.plaphy.2004.03.003)
- Lin N, Dufresne A (2014a) Surface chemistry, morphological analysis and properties of cellulose nanocrystals with gradiented sulfation degrees. *Nanoscale*. doi:[10.1039/C3NR06761K](https://doi.org/10.1039/C3NR06761K)
- Lin N, Dufresne A (2014b) Surface chemistry, morphological analysis and properties of cellulose nanocrystals with gradiented sulfation degrees. *Nanoscale* 6:5384–5393. doi:[10.1039/C3NR06761K](https://doi.org/10.1039/C3NR06761K)
- Lopez M et al (2010) Enthalpic studies of xyloglucan–cellulose interactions. *Biomacromolecules* 11:1417–1428. doi:[10.1021/bm1002762](https://doi.org/10.1021/bm1002762)
- Marchessault RH, Morehead FF, Walter NM (1959) Liquid crystal systems from fibrillar polysaccharides. *Nature* 184:632–633
- Martínez-Sanz M, López-Rubio A, Lagaron JM (2011) Optimization of the nanofabrication by acid hydrolysis of bacterial cellulose nanowhiskers. *Carbohydr Polym* 85:228–236. doi:[10.1016/j.carbpol.2011.02.021](https://doi.org/10.1016/j.carbpol.2011.02.021)
- McNeil M, Darvill AG, Fry SC, Albersheim P (1984) Structure and function of the primary cell walls of plants. *Annu Rev Biochem* 53:625–663. doi:[10.1146/annurev.bi.53.070184.003205](https://doi.org/10.1146/annurev.bi.53.070184.003205)
- Mellerowicz EJ, Immerzeel P, Hayashi T (2008) Xyloglucan: the molecular muscle of trees. *Ann Bot* 102:659–665. doi:[10.1093/aob/mcn170](https://doi.org/10.1093/aob/mcn170)
- Morris S, Hanna S, Miles MJ (2004) The self-assembly of plant cell wall components by single-molecule force spectroscopy and Monte Carlo modelling. *Nanotechnology* 15:1296

- Nogi M, Yano H (2008) Transparent nanocomposites based on cellulose produced by bacteria offer potential innovation in the electronics device industry. *Adv Mater* 20:1849–1852. doi:[10.1002/adma.200702559](https://doi.org/10.1002/adma.200702559)
- Ogawa K, Hayashi T, Okamura K (1990) Conformational analysis of xyloglucans. *Int J Biol Macromol* 12:218–222
- Oksman K, Mathew AP, Bondeson D, Kvien I (2006) Manufacturing process of cellulose whiskers/polylactic acid nanocomposites. *Compos Sci Technol* 66:2776–2784. doi:[10.1016/j.compscitech.2006.03.002](https://doi.org/10.1016/j.compscitech.2006.03.002)
- Palik ED (1985) Handbook of optical constants of solids. Orlando, Florida
- Parikka K et al (2012) Functional and anionic cellulose-interacting polymers by selective chemo-enzymatic carboxylation of galactose-containing polysaccharides. *Biomacromolecules* 13:2418–2428. doi:[10.1021/bm300679a](https://doi.org/10.1021/bm300679a)
- Ramos LP, Nazhad MM, Saddler JN (1993) Effect of enzymatic hydrolysis on the morphology and fine structure of pre-treated cellulosic residues. *Enzyme Microb Technol* 15:821–831. doi:[10.1016/0141-0229\(93\)90093-H](https://doi.org/10.1016/0141-0229(93)90093-H)
- Ranby BG, Banderet A, Sillén LG (1949) Aqueous colloidal solutions of cellulose micelles. *Acta Chem Scand* 3:649–650
- Shirakawa M, Yamatoya K, Nishinari K (1998) Tailoring of xyloglucan properties using an enzyme. *Food Hydrocoll* 12:25–28. doi:[10.1016/S0268-005X\(98\)00052-6](https://doi.org/10.1016/S0268-005X(98)00052-6)
- Souza Lima MM, Borsali R (2004) Rodlike cellulose microcrystals: structure, properties, and applications. *Macromol Rapid Commun* 25:771–787. doi:[10.1002/marc.200300268](https://doi.org/10.1002/marc.200300268)
- Souza CF, Lucyszyn N, Woehl MA, Riegel-Vidotti IC, Borsali R, Sierakowski MR (2013) Property evaluations of dry-cast reconstituted bacterial cellulose/tamarind xyloglucan biocomposites. *Carbohydr Polym* 93:144–153
- Sugiyama J, Vuong R, Chanzy H (1991) Electron diffraction study on the two crystalline phases occurring in native cellulose from an algal cell wall. *Macromolecules* 24:4168–4175. doi:[10.1021/ma00014a033](https://doi.org/10.1021/ma00014a033)
- Sze A, Erickson D, Ren L, Li D (2003) Zeta-potential measurement using the Smoluchowski equation and the slope of the current–time relationship in electroosmotic flow. *J Colloid Interface Sci* 261:402–410. doi:[10.1016/s0021-9797\(03\)00142-5](https://doi.org/10.1016/s0021-9797(03)00142-5)
- Taylor IEP, Atkins EDT (1985) X-ray diffraction studies on the xyloglucan from tamarind (*Tamarindus indica*) seed. *FEBS Lett* 181:300–302. doi:[10.1016/0014-5793\(85\)80280-5](https://doi.org/10.1016/0014-5793(85)80280-5)
- Whitney SEC, Brigham JE, Darke AH, Reid JSG, Gidley MJ (1995) In vitro assembly of cellulose/xyloglucan networks: ultrastructural and molecular aspects. *Plant J* 8:491–504. doi:[10.1046/j.1365-313X.1995.8040491.x](https://doi.org/10.1046/j.1365-313X.1995.8040491.x)
- Whitney SEC, Gothard MGE, Mitchell JT, Gidley MJ (1999) Roles of cellulose and xyloglucan in determining the mechanical properties of primary plant cell walls. *Plant Physiol* 121:657–664. doi:[10.1104/pp.121.2.657](https://doi.org/10.1104/pp.121.2.657)
- Winter HT, Cerclier C, Delorme N, Bizot H, Quemener B, Cathala B (2010) Improved colloidal stability of bacterial cellulose nanocrystal suspensions for the elaboration of spin-coated cellulose-based model surfaces. *Biomacromolecules* 11:3144–3151. doi:[10.1021/bm100953f](https://doi.org/10.1021/bm100953f)
- Woehl MA, Canestraro CD, Mikowski A, Sierakowski MR, Ramos LP, Wypych F (2010) Bionanocomposites of thermoplastic starch reinforced with bacterial cellulose nanofibres: effect of enzymatic treatment on mechanical properties. *Carbohydr Polym* 80:866–873. doi:[10.1016/j.carbpol.2009.12.045](https://doi.org/10.1016/j.carbpol.2009.12.045)
- Yang D-Q, Xiong Y-Q, Guo Y, Da D-A, Lu W-G (2001) Sizes correction on AFM images of nanometer spherical particles. *J Mater Sci* 36:263–267. doi:[10.1023/A:1004894532155](https://doi.org/10.1023/A:1004894532155)
- York WS, Kolli VSK, Orlando R, Albersheim P, Darvill AG (1996) The structures of arabinoxyloglucans produced by solanaceous plants. *Carbohydr Res* 285:99–128. doi:[10.1016/S0008-6215\(96\)90176-7](https://doi.org/10.1016/S0008-6215(96)90176-7)
- Yu H, Qin Z, Liang B, Liu N, Zhou Z, Chen L (2013) Facile extraction of thermally stable cellulose nanocrystals with a high yield of 93 % through hydrochloric acid hydrolysis under hydrothermal conditions. *J Mater Chem A* 1:3938–3944. doi:[10.1039/C3TA01150J](https://doi.org/10.1039/C3TA01150J)
- Zhang J, Elder TJ, Pu Y, Ragauskas AJ (2007) Facile synthesis of spherical cellulose nanoparticles. *Carbohydr Polym* 69:607–611. doi:[10.1016/j.carbpol.2007.01.019](https://doi.org/10.1016/j.carbpol.2007.01.019)
- Zhao Z, Crespi V, Kubicki J, Cosgrove D, Zhong L (2014) Molecular dynamics simulation study of xyloglucan adsorption on cellulose surfaces: effects of surface hydrophobicity and side-chain variation. *Cellulose* 21:1025–1039. doi:[10.1007/s10570-013-0041-1](https://doi.org/10.1007/s10570-013-0041-1)
- Zhou Q, Rutland M, Teeri T, Brumer H (2007) Xyloglucan in cellulose modification *Cellulose* 14:625–641. doi:[10.1007/s10570-007-9109-0](https://doi.org/10.1007/s10570-007-9109-0)
- Zykwinska A, Thibault J-F, Ralet M-C (2008) Modelling of xyloglucan, pectins and pectic side chains binding onto cellulose microfibrils. *Carbohydr Polym* 74:23–30. doi:[10.1016/j.carbpol.2008.01.011](https://doi.org/10.1016/j.carbpol.2008.01.011)